A SENSITIVE SEARCH FOR VARIABILITY IN LATE L DWARFS: THE QUEST FOR WEATHER

M. Morales-Calderón,[1,2] J. R. Stauffer,[3] J. Davy Kirkpatrick,[4] S. Carey,[3] C. R. Gelino,[3]
D. Barrado y Navascués,[1] L. Rebull,[3] P. Lowrance,[3] M. S. Marley,[5]
D. Charbonneau,[6,7] B. M. Patten,[6] S. T. Megeath,[6] and D. Buzasi[8]

ABSTRACT

We have conducted a photometric monitoring program of three field late L brown dwarfs (DENIS-P J0255−4700, 2MASS J0908+5032, and 2MASS J2244+2043) looking for evidence of nonaxisymmetric structure or temporal variability in their photospheres. The observations were performed using *Spitzer* IRAC 4.5 and 8 μm bandpasses and were designed to cover at least one rotational period of each object; 1 σ rms uncertainties of less than 3 mmag at 4.5 μm and around 9 mmag at 8 μm were achieved. Two out of the three objects studied exhibit some modulation in their light curves at 4.5 μm—but not 8 μm—with periods of 7.4 hr (DENIS 0255) and 4.6 hr (2MA 2244) and peak-to-peak amplitudes of 10 and 8 mmag. Although the lack of detectable 8 μm variation suggests an instrumental origin for the detected variations, the data may nevertheless still be consistent with intrinsic variability, since the shorter wavelength IRAC bandpasses probe more deeply into late L dwarf atmospheres than the longer wavelengths. A cloud feature occupying a small percentage (1%–2%) of the visible hemisphere could account for the observed amplitude of variation. If, instead, the variability is indeed instrumental in origin, then our nonvariable L dwarfs could be either completely covered with clouds or objects whose clouds are smaller and uniformly distributed. Such scenarios would lead to very small photometric variations. Follow-up IRAC photometry at 3.6 and 5.8 μm bandpasses should distinguish between the two cases. In any event, the present observations provide the most sensitive search to date for structure in the photospheres of late L dwarfs at mid-IR wavelengths, and our photometry provides stringent upper limits to the extent to which the photospheres of these transition L dwarfs are structured.

Subject headings: stars: individual (DENIS-P J0255−4700, 2MASS J0908+5032, 2MASS J2244+2043) —
stars: low-mass, brown dwarfs — stars: variables: other

1. INTRODUCTION

The onslaught of L and T dwarf discoveries within in the last 10 years has enabled direct comparisons between observations and modeling of brown dwarf cooling tracks. The transition region from the late L dwarfs to the early T dwarfs has always been problematic for brown dwarf atmosphere modelers. First among the unanswered questions relates to the fact that early T dwarfs tend to have absolute *J* magnitudes brighter than later L dwarfs, the so-called *J*-band bump (Vrba et al. 2004). Further problems arise from the large dispersion of certain colors as a function of spectral type (Knapp et al. 2004) as well as the discrepancies between the optical and near-IR derived spectral types of some transition objects (Kirkpatrick 2005). Although some of these issues can be answered with unresolved binaries (Liu 2006), it is also likely true that the mechanism for dust clearing is intimately involved in the explanation of all of these observables. At least three mechanisms for dust clearing have been proposed: (1) the cloud deck thins and sinks, eventually dropping below the photosphere (Tsuji & Nakajima 2003); (2) the cloud deck breaks up into discrete (patchy) clouds, and eventually those clouds either shrink or sink below the visible photosphere (Burgasser et al. 2002); and (3) a "sudden downpour" (rapid sedimentation period) occurs, rapidly removing grains from the visible photosphere (Knapp et al. 2004).

Photometric variability is one observable that may be able to provide constraints on which of these mechanisms, if any, is the dominant process occurring in very cool atmospheres. The atmospheres of these objects are too cool and neutral to support star spots (Mohanty & Basri 2003; Gelino et al. 2002), so if variability exists, it is most likely caused by nonuniform structures in the cloud deck. If the objects are not variable, then either the variability is below the limits of detection, or the cloud decks are uniformly distributed over the entire atmosphere, leaving no features to produce brightness variations.

Numerous attempts have been made to search for photometric variability in L and T dwarfs. These searches for "weather" have been performed largely in the optical regime (Tinney & Tolley 1999; Bailer-Jones & Mundt 1999, 2001; Clarke et al. 2002a, 2002b; Gelino 2002; Gelino et al. 2002; Koen 2003, 2005; Maiti et al. 2005) and the near-IR (Bailer-Jones 2002; Gelino 2002; Bailer-Jones & Lamm 2003; Enoch et al. 2003; Koen et al. 2004, 2005). The results of these surveys indicate that the photometric variability of these objects falls under one of three categories: nonvariable, periodic variable, and nonperiodic variable. Objects that show no variations generally have limits of a few percent. Those that show nonperiodic variations have rms amplitudes of a few percent and vary on timescales too short to be correlated with a rotation period (Bailer-Jones & Mundt 2001; Gelino et al. 2002; Bailer-Jones 2004). The small fraction that appear to show periodic modulation of their light curves have typical amplitudes

[1] Laboratorio de Astrofísica Espacial y Física Fundamental (LAEFF-INTA), P.O. Box 50727, E-28080 Madrid, Spain; mariamc@laeff.inta.es.
[2] Visiting Graduate Student Fellow at the *Spitzer* Science Center, California Institute of Technology, Pasadena, CA 91125.
[3] *Spitzer* Science Center, California Institute of Technology, Pasadena, CA 91125.
[4] Infrared Processing and Analysis Center, California Institute of Technology, Pasadena, CA 91125.
[5] NASA Ames Research Center, Moffett Field, CA 94035.
[6] Harvard-Smithsonian Center for Astrophysics, Cambridge, MA 02138.
[7] Alfred P. Sloan Research Fellow.
[8] US Air Force Academy, Colorado Springs, CO 80840.

TABLE 1
LATE L DWARF TARGETS

Object	Optical Spectral Type	Near-IR Spectral Type	$J-K_s$[a]	$v \sin i$ (km s^{-1})	References
DENIS 0255	L8	. . .	1.69 ± 0.050	40 ± 10	1, 5
2MA 0908..................	L5	L9 ± 1	1.60 ± 0.051	31	2, 4, 6
2MA 2244..................	L6.5	L7.5 ± 2	2.45 ± 0.213	. . .	3, 4

[a] The $J-K_s$ colors come from the 2MASS magnitudes.
REFERENCES.—(1) J. D. Kirkpatrick et al. 2006, in preparation; (2) Cruz et al. 2003; (3) Dahn et al. 2002; (4) Knapp et al. 2004; (5) Basri et al. 2000; (6) D. Charbonneau (2006, private communication).

of a few percent and periods usually of order several hours. The fact that the light curves in several cases appear roughly sinusoidal suggests high-latitude features; low-latitude features (i.e., those near the equator) would likely be eclipsed when on the far side of the object, resulting in a flat section in the light curve, and this is not observed.[9] Another explanation would be that the clouds are distributed on the surface so that one hemisphere is cloudier than the other: that is, we are seeing changes in the cloud covering as the brown dwarf rotates.

The limiting factors in the photometric accuracy of these surveys are the intrinsic faintness of the targets in the optical and second-order extinction effects from the Earth's atmosphere in the near-IR (Bailer-Jones & Lamm 2003). In both cases, the usual single measurement 1 σ uncertainties is of order the amplitude of the quoted variability. This effect could be responsible for objects appearing variable in one survey, but not in others (Bailer-Jones & Mundt 2001; Gelino et al. 2002). It is also possible that some claims of variability in L dwarfs are spurious and instead are the result of higher than expected photometric errors. Only highly precise photometric observations can resolve such issues.

We have conducted a program with the Infrared Array Camera (IRAC) on the *Spitzer Space Telescope* to search for photometric variations in a small sample of late L dwarfs near the L/T transition. In § 2 we describe briefly the target selection. Section 3 describes the observational strategy used to accomplish the desired accuracy level. Sections 4 and 5 deal with the data reduction and the correction of the instrumental effects found in our data, and § 6 describes briefly the variability and periodogram tests that we have used. We present the results for each target in § 7 and finally summarize our findings in § 8.

2. TARGET SELECTION

Our sample consists of three late L field brown dwarfs near the L/T transition. Two of them were selected based on having a large $v \sin i$, and hence a period easy to cover with a few hours of continuous monitoring, and the third was selected based on NIR colors. The principal characteristics of these objects are shown in Table 1, and their IRAC magnitudes are shown in Table 4.

DENIS-P J0255−4700 (hereafter DENIS 0255) is an L8 brown dwarf (J. D. Kirkpatrick et al. 2006, in preparation) at approximately 5.0 pc. It is one of the brightest members of the so-called late L/early T transition objects that are the subject of this work. This object has a $v \sin i$ of 40 ± 10 km s^{-1} measured by Basri et al. (2000) and $v \sin i$ of 40.8 ± 8.0 or 41.1 ± 2.8 km s^{-1} measured by Zapatero Osorio et al. (2006). For an object of radius 0.1 $R_\odot$, as expected for brown dwarfs (Chabrier & Baraffe 1997), a ro-

tational velocity of 40 km s^{-1} corresponds to a rotation period of 3 hr; this is an upper limit due to the unknown inclination of the rotation axis to the line of sight.

The second object, 2MASS J0908+5032 (hereafter 2MA 0908) is one of a handful of L dwarfs with very discrepant optical and near-infrared spectral types. In the optical its type is L5 (Cruz et al. 2003), but its near-infrared type is much later, L9 ± 1 (Knapp et al. 2004). The late near-infrared type could be indicative of a cloudy atmosphere, while the optical type indicates a temperature warmer than the average, a very dusty dwarf. This object has a measured $v \sin i$ of 31 km s^{-1} (D. Charbonneau 2006, personal communication), so its period should be less than 4 hr.

The last object, 2MASS J2244+2043 (hereafter 2MA 2244), is a brown dwarf with a spectral type of L7.5 ± 2 (Knapp et al. 2004). Although its $v \sin i$ has not been measured, it was selected as a target because it is among the reddest known L or T dwarfs in the near-infrared colors ($J-K_s = 2.45$). As such, it is believed to be exceedingly dusty and thus a prime candidate for this work. Based on the average $v \sin i$ (in the range 20–40 km s^{-1}) of L dwarfs of similar type (Basri et al. 2000; Mohanty & Basri 2003; Bailer-Jones 2004; Zapatero Osorio et al. 2006), we expect a rotational period of approximately 6.5 hr or less.

3. OBSERVATIONS

The goal of our program was to obtain well-sampled relative photometry for our target objects for time periods longer than their expected rotational period. We hoped to be able to do both temporal relative photometry (i.e., how the measured flux of our target objects varied with time during the observation) and differential relative photometry (i.e., how the brightness of our targets varied as compared to another comparison object in our field of view). In general, the comparison stars we had hoped to use proved to be fainter than expected, making their photometry less accurate, and for that reason most of the results we report will simply be for the temporal relative photometry of the brown dwarf itself.

IRAC has four separate cameras, and data are collected in all four channels (3.6, 4.5, 5.8, and 8.0 μm) for the standard Astronomical Observation Request (AOR). The detector arrays have been shown to be very stable, with very little variation in the flux calibration over the entire time *Spitzer* has been in orbit (Fazio et al. 2004; Reach et al. 2005). IRAC is also very sensitive and is capable of obtaining enough photons for millimagnitude photometry in at least Channels 1 and 2 (hereafter Ch. 1, Ch. 2, etc.) for all of our targets with integration times of 100 s or less. Given these expectations, the primary limitations for temporal relative photometry would come from flat-field errors and other pixel-to-pixel effects. This suggests that an observing mode in which the spacecraft simply stares at the target object, with no dithering, should provide the most accurate relative photometry. This expectation has been confirmed by the recent usage of IRAC to measure the depth of the planet transit in the Transatlantic Exoplanet

---

[9] Gelino et al. (2002) observed a significant dip occurring over 10 days in the generally flat light curve of the L1 dwarf 2MASS 1300+1912. The duration of this feature is much longer than the expected rotation period of an L dwarf (a few hours; Basri et al. 2000; Bailer-Jones 2004) and possibly reflects the creation and subsequent dissipation of a large storm.

TABLE 2
OBSERVING STRATEGY

Object	Observation Date (UT)	Number of AORs	Number of Repeats	Frame Time (s)	Time on Target (hr)
DENIS 0255	24 Aug 2005	6	255	12	6
2MA 0908...................	29 Nov 2005	1	890	30	7.7
2MA 2244...................	29 Nov 2005	2	104	100	6.5

Survey 1 (TrES-1) (Charbonneau et al. 2005), where relative photometry with rms accuracies of 0.5 and 1.5 mmag were demonstrated for Ch. 2 and Ch. 4, respectively. These levels of uncertainties are an order of magnitude better than what ground-based weather searches have accomplished and, even though our targets are significantly fainter than TrES-1 (and thus the accuracy will be lower), can provide very constrained limits on the amplitudes of photometric variations in our targets. We therefore chose to use the staring mode for our brown dwarf weather program.

The four IRAC channels do not simultaneously view the same position on the sky, however: Ch. 1 and 3 view one field of view, and Ch. 2 and 4 view another nonoverlapping but approximately adjacent field of view. If we are to stare at our target object, therefore, we must choose which field of view to use. From an astrophysical point of view, the choice was not clear-cut: there was no empirical data from previous IRAC or ground-based observations to suggest that variability would be greater in one filter pair, nor was there compelling guidance from the theoretical models. We therefore chose to use the same filter pair (Ch. 2 and 4), as had been used for the planet transit observations. One reason for this is that Ch. 2 is the most sensitive and the most well behaved (e.g., "pixel-phase" effects are thought to be smaller in Ch. 2 than Ch. 1; see § 5.1), suggesting that better relative photometry should be possible with Ch. 2.

If no other constraints were involved, the observations for our targets would therefore have been extremely simple to describe: slew to the target and center it in the Ch. 2/4 field of view, wait until the spacecraft pointing has settled, and take N consecutive frames of data with integration time M. Table 2 summarizes the different settings adopted for each target: observation date, number of AORs, number of consecutive images taken in each AOR, integration time per pixel, and total time on target for each observed object. The integration time is selected so that the number of electrons in the central pixel is not too large (~half-full well, so that linearity corrections are small; see the IRAC Data Handbook);[10] the number of consecutive frames is set so that the total time on target is significantly greater than the expected rotation period. For our first and brightest target, DENIS 0255, however, one additional constraint caused us to deviate significantly from this simple procedure. At the time we constructed the observing plan for DENIS 0255, a single AOR was limited to 256 repeated exposures. Because DENIS 0255 is relatively bright, the maximum exposure time we could use was 12 s; hence, a single AOR was limited to of order an hour. With a desired 6 hr on target, we therefore had to break up our observation into six consecutive AORs. The only difficulty with this is that the AOR is defined such that it begins with a slew to the target and a reacquisition by the star tracker, and we could not eliminate that process. Therefore, even though for the second through sixth AORs we were already pointed at the target, there was still a brief acquisition sequence and a consequent slight repointing of the spacecraft, and thus a repositioning of the target on the arrays at the start of each AOR.

For 2MA 2244, which is much fainter than DENIS 0255, the individual exposure time was instead 100 s, and therefore we were able to observe the target for 6.5 hr with only two AORs. Due to the background brightness in Ch. 4, the maximum exposure time in this bandpass is 50 s. Hence, we had two 50 s exposures in Ch. 4 per each 100 s exposure in Ch. 2 (104 repeat exposures per AOR in Ch. 2 and 208 in Ch. 4). For 2MA 0908, we were able to avoid these recenterings of the spacecraft. In this case, we conducted the observations in an engineering mode that had no limit on the number of repeat exposures, and hence the observation was conducted with essentially a single AOR and only the initial spacecraft pointing acquisition.

4. DATA ANALYSIS

Our starting point for the data analysis was the Basic Calibrated Data (BCD) produced by the IRAC pipeline software (ver. S13.0.1) at the *Spitzer* Science Center (SSC). The tasks performed by the pipeline are mainly dark subtraction, multiplexer bleed correction, detector linearization, flat fielding, cosmic-ray detection, and finally flux calibration. For a detailed description of these processes, see the IRAC Data Handbook. This pipeline is intended to produce fully flux-calibrated images that have had most of the well-understood instrumental signatures removed. However, there are some instrumental effects that are not corrected; we take a close look at them in § 5. The BCD images are calibrated in units of MJy sr^{-1}. Calibrated magnitudes were obtained using the zero-point fluxes and transforming them into magnitudes to obtain the appropriate BCD zero-point magnitude for each channel. The BCD plate scale used to obtain the zero magnitudes is 1″22 pixel^{-1}, and the zero points used in the calibration are listed in Table 3.

The finding of a good centroiding and the photometry extraction were performed under IRAF standard procedures. Both STARFIND and DAOFIND routines were used for the source extraction because, probably due to the pixel-phase effect and the IRAC undersampling, the routine to derive pixel coordinates within DAOFIND produced results that were sometimes inaccurate (see § 5). We performed aperture photometry using PHOT with a source aperture of 4 pixel radius (4″88). The aperture radius was selected in order to obtain the maximum signal-to-noise ratio. The sky background was subtracted using an annulus with inner radius of 15 pixels (18″3) and width of 10 pixels (12″2). We selected this relatively large sky annuli to provide the best possible subtraction of background given the lack of objects close

---

[10] See http://ssc.spitzer.caltech.edu/irac/dh/iracdatahandbook3.0.pdf.

TABLE 3
ZERO-MAGNITUDE FLUX FOR IRAC

IRAC Channel/Wavelength (μm)	Flux at Zero Magnitude (Jy)	Zero-Point Magnitude (mag)
Ch. 2/4.5	179.7	16.78
Ch. 4/8.0	64.1	15.65

to the targets in our images. The IRAC calibration aperture has a 10 native pixel radius, and thus we had to apply an aperture correction to our data. We derived additive aperture corrections in magnitudes of 0.094 and 0.097 mag for Ch. 2 and Ch. 4, respectively, directly from our own observations.

To compute random errors for our light curves, we assumed that no significant real variability in our objects occurs on timescales of 20 minutes or less. We measured the scatter of every 10 data points (5 data points for the faintest object because of the longer exposure time), and the 1 σ error bars in the figures represent the median of these values. Thus, the errors in the light curves were computed empirically from the data themselves. We make no estimate of the systematic error in our absolute fluxes because our observing mode is not designed to provide the best absolute fluxes (we are staring at the target instead of dithering).

An example of the raw light curves for one of our objects, DENIS 0255, can be seen in Figure 1a, in which only the very large, isolated deviants have been removed ($\sim$2% of the data points, presumably cosmic-ray hits). The Ch. 2 data do show some variation, but because the changes happen at AOR boundaries, we suspect an instrumental cause. In order to improve the signal-to-noise ratio, the BCD images were combined in groups. We selected five as the number of images to combine in each group for our final analysis as a trade-off between maximizing the signal-to-noise ratio of source flux (see Fig. 1b) while at the same time preserving temporal resolution. Therefore, we have 300 merged data points with 1 minute increments spanning almost 6 hr of observation time for the first target, DENIS 0255. For 2MA 0908, the observations were taken under only one AOR spanning approximately 8 hr. After combining the images, we had 178 data points in increments of 2.5 minutes. Finally, we have 42 data points in 8.3 minute increments for the faintest target, 2MA 2244, which was observed for 6.5 hr in two different AORs. Because we have twice as many images in Ch. 4 (half-exposure time each) as in Ch. 2 (see § 3), we combined the images in groups of 10 for the Ch. 4 data to match the time increment in both channels. We have at least one field object per target, and they were analyzed in exactly the same way as the science targets. However, we did not perform differential photometry because, even though the 2MASS K_s magnitudes of the field objects were comparable to those of our targets, their IRAC magnitudes were significantly fainter (between 1 and 3 mag fainter), and therefore their light curves were much noisier. We did use them as control objects, comparing their time series with the science ones.

The time series for the averaged data points for our three targets in both bandpasses can be seen in Figure 2. The top panels are the light curves for Ch. 2, extracted as explained above, and the bottom ones are for the Ch. 4 data. In these time series, without any possible corrections applied, we see no evidence of a rotational variability (at least in DENIS 0255 and 2MA 0908). Upper limits on the intrinsic variability of our targets at Ch. 2 and Ch. 4 bandpasses were established as the rms of the light curves. Therefore, if any sinusoidal variation is present, its rms amplitude would be below 5, 3, and 4 mmag for DENIS 0255, 2MA 0908, and 2MA 2244, respectively, in Ch. 2, and below 6, 10, and 6 mmag in Ch. 4.

The Ch. 2 data do show photometric variations, particularly in DENIS 0255, as illustrated in the top left panel of Figure 2. Those variations are clearly correlated with the change with time of the star's centroid position (see Fig. 3) and are the most noticeable in DENIS 0255, with a maximum amplitude of 1%–2%. The light curve of this object exhibits some large discontinuities that occur at the transition from one AOR to the next. The correlation between centroid position and photometric variations
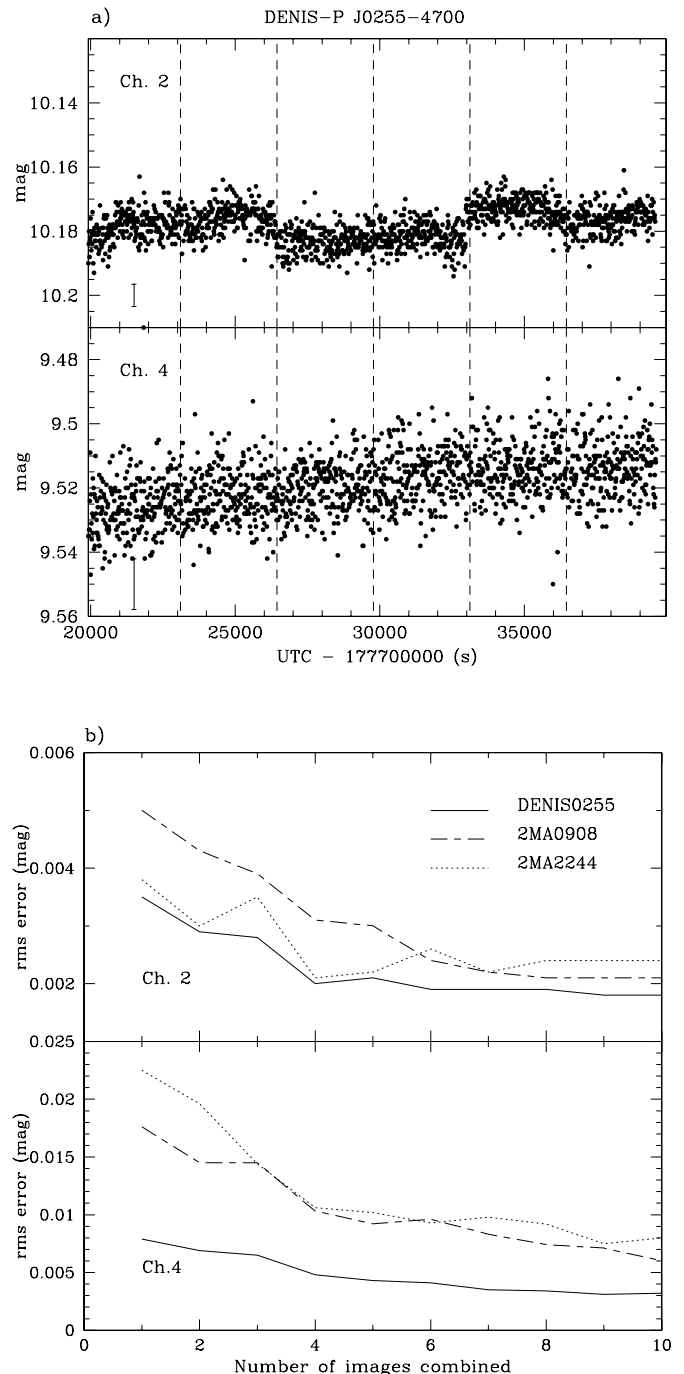

Fig. 1.—(a) Raw light curve for DENIS 0255. The top and bottom panels show the Ch. 2 and Ch. 4 time series, respectively, and the vertical dashed lines delimit the different AORs. The 1 σ uncertainty per point is represented in the lower left corner of each panel. (b) Dependence of the dispersion about the mean on the number of data points combined for DENIS 0255 (*solid lines*), 2MA 0908 (*dashed lines*), and 2MA 2244 (*dotted lines*). Note that the scales are different in the two panels.

is not so obvious for the two fainter objects, but this is probably due to the fact that their movement is much smaller: <0.1 pixels for 2MA 0908 and around 0.3 pixels for 2MA 2244. Looking at the centroid position versus time, the pointing jitter is very small inside a single AOR, but offsets as large as 0.7 pixels occurred along the whole observation period due to the reacquisition of guide stars at the beginning of each observation. In the case of DENIS 0255, we also found a large drift, about 0.2 pixels (0″.24) in the target's y-position on the array during the first 20 minutes
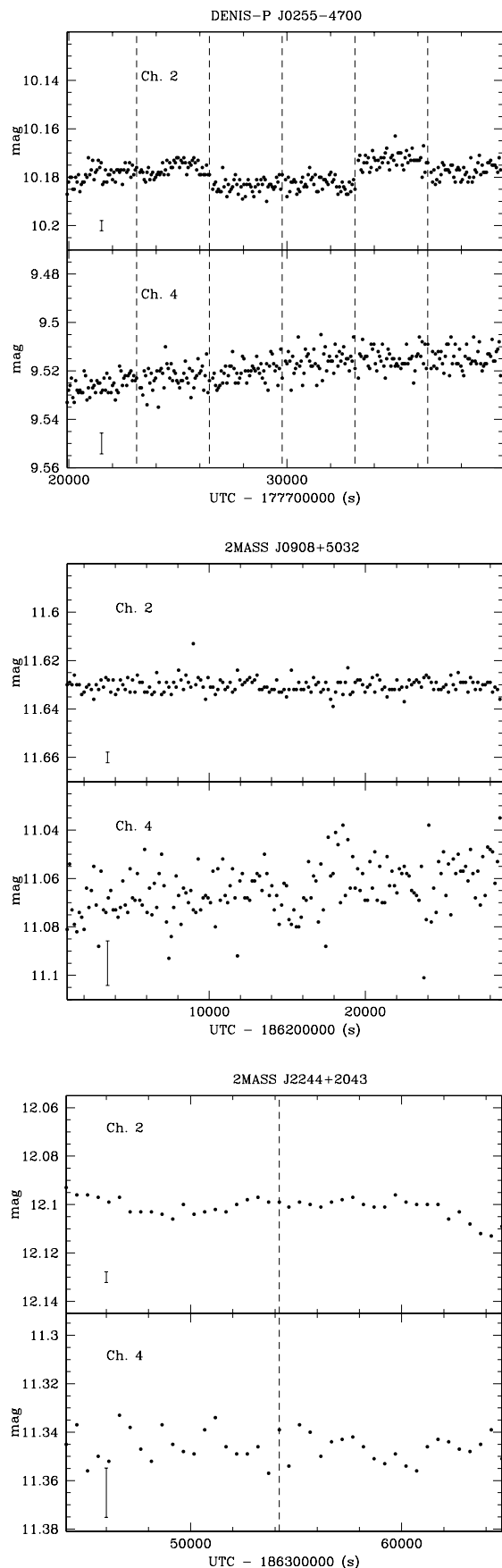
FIG. 2.—Light curves for DENIS 0255, 2MA 0908, and 2MA 2244 obtained from the binned data. The top and bottom panels show Ch. 2 and Ch. 4 time series, respectively. The rms uncertainty of a single binned point is represented in the lower left corner of each panel. The vertical dashed lines delimit the different AORs.
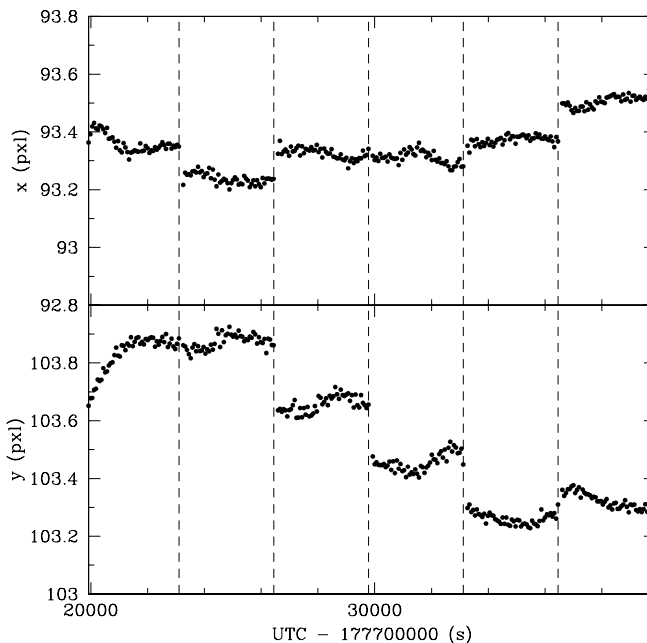

FIG. 3.—STARFIND centroid position as a function of time for DENIS 0255. The x- and y-positions are shown at the top and the bottom panels, respectively. The vertical dashed lines denote the boundaries between AORs. The spacecraft re-acquires guide stars at the start of an AOR, causing the disjointed jumps in position.

of the first AOR. (See § 5.4 for a further discussion of the pointing variations and their influence on the Ch. 2 photometry.)

The first step in deriving time series photometry is the determination of the centroid positions for the target star in each image. We initially used DAOFIND for this purpose, but noted odd shifts (large shifts and even bimodal positions) in the centroids for some images that we believed to be spurious. We wrote a simple first-moment routine to check the DAOFIND centroids, which worked better with the centroiding but was relatively noisy. We finally settled on the STARFIND routine, which we believe returns good centroids for nearly all of the images. The undersampling in the Ch. 2 makes the centroid determinations relatively inaccurate even for STARFIND, but we do not believe the trends in the light curves are a result of this imprecision. If the photometric variations were primarily attributable to errors in the centroiding, increasing the aperture size would have helped. However, we found a similar trend using bigger apertures, with the only difference being noisier light curves depending on the aperture we used. Moving the sky annulus farther out did not remove the effect either.

The discontinuities in the Ch. 2 photometry at AOR boundaries could also be due to pixel-to-pixel flat-field errors in combination with the position shifts illustrated in Figure 3. We examined the flat field used, and there are differences in the values of the flat field of order 2% between different pixels near the location of DENIS 0255 that could, in principle, cause the photometric shifts we see in Figure 2. As a test of this, we extracted photometry from the raw data frames and found a light curve very similar to that derived from the BCD data. This does not completely exclude flat-field errors as the cause of the variations seen for DENIS 0255 in Figure 2, but we believe this is not a significant contributor.

The Ch. 4 data do not show the same photometric variations as the Ch. 2 data. Instead, DENIS 0255 and 2MA 0908, the two brightest objects, show brightening of 1.5% along the whole observation period. We discuss this effect in § 5.2.

5. INSTRUMENTAL EFFECTS AND CORRECTIONS

5.1. *Pixel-Phase Effect*

The number of electrons created in the image of a star in IRAC Ch. 1 and Ch. 2 depends on exactly how the star is centered relative to the center of a pixel. This effect is probably the result of light losses at the boundaries between pixels. It is repeatable, and there is a quasi-linear relation between what we measure as the magnitude and the displacement from the center of the pixel. Therefore, a star whose image is centered on the center of a pixel has the maximum apparent flux, while a star centered on the interstices of 4 pixels has the minimum apparent flux. This effect is called the pixel-phase effect, and more information is available in the IRAC Data Handbook.

This artifact results in a variation in the detected flux of an object as its image moves relative to the center of a pixel. The lack of a detectable pixel-phase effect for IRAC Ch. 3 and Ch. 4 is probably due to their use of a different detector technology (SiAs vs. InSb) and to the broader PSFs for the longer wavelength channels.

The SSC provides a functional form for the correction for pixel-phase effect for Ch. 1 on its Web site. Pixel phase is defined as the distance of the centroid position of a star from the center of the pixel with the most flux; thus,

$$\text{phase} = \sqrt{(x - x_0)^2 + (y - y_0)^2}, \tag{1}$$

where, for each image, x, y are the positions of the source's centroid and x_0, y_0 are the integer pixel numbers containing the source centroid. The correction for Ch. 1 is defined as a linear relation in flux:

$$\text{correction} = 1 + 0.0535 \left(\frac{1}{\sqrt{2\pi}} - \text{phase} \right). \tag{2}$$

The SSC does not provide a similar formula for Ch. 2 because the scatter in the data available to calibrate the effect is comparable to the effect. The Formation and Evolution of Planetary Systems (FEPS) legacy team has also examined their IRAC BCD images for >300 nearby F-, G-, and K-type dwarfs for pixel-phase effects. They find a very similar relation for Ch. 1 to that provided by the SSC. For Ch. 2, they also find ambiguous data. For some positions on the array, they see a similar pixel-phase relation as for Ch. 1; at other positions, they see no obvious pixel-phase effect (Meyer et al. 2004).

We chose to assume that a pixel-phase effect might be present in our Ch. 2 data and to determine empirically the size of the effect (the slope of the relation between pixel phase and flux). We modeled the effect as a linear relation between flux and pixel phase, varied the slope of the relation from 0.00 to 0.07, and examined the light curves for our three L dwarfs and the field objects for each choice of slope. We assumed that the slope that minimized the discontinuities in the photometry between the AORs was correct. This led us to a slope of 0.05—very similar to what is found in Ch. 1. Figure 4 shows the light curves for DENIS 0255 for several different choices of the slope to the pixel-phase correction formula.

5.2. *Latent Image Charge Buildup*

The two brightest objects of our sample show an upward trend in brightness of 1.5% from the beginning to the end of the observation at Ch. 4 (see Fig. 2). The shape of the light curves is
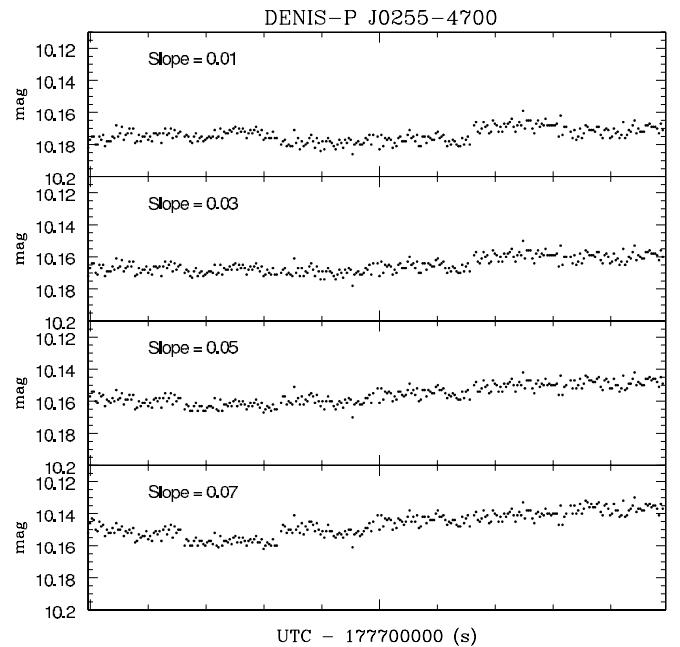

FIG. 4.—Different pixel-phase-corrected light curves for DENIS 0255 depending on the slope adopted in the pixel-phase correction. We adopted a slope of 0.05 as the best one.

very different from what we see in Ch. 2 and, if real and interpreted as rotational modulation, would imply periods much longer than those inferred from the spectroscopic rotational velocities. We believe instead that what we are seeing in the Ch. 4 data is a latent image buildup. This effect was also observed in Charbonneau et al. (2005), where the target and calibrators were brighter than our targets.

This instrumental effect may depend on the flux of the target. In addition, there is a pixel-dependent term in the behavior of the long-term latents, and it is possible that they are frame time dependent. Despite that, and even though the nonvariable calibrators in Charbonneau et al. (2005) data are brighter than our targets, there is no other data set more similar to ours in terms of time staring to an object, so we decided to use their calibrators to correct the photometry of our targets in Ch. 4. We reanalyzed their BCDs, extracted the photometry, and used the normalized flux to fit a second-degree polynomial to each calibrator. Then the time series of DENIS 0255 and 2MA 0908 were divided by the mean of both fittings.

The functional form for this correction is

$$\text{correction} = \left(-2.2402 \times 10^{-11}\right) t^2 + \left(1.1872 \times 10^{-6}\right) t + 0.9917, \tag{3}$$

$$\text{corrected flux} \, (\text{MJy sr}^{-1}) = \text{flux/correction}, \tag{4}$$

where t is the time (in seconds) when the exposure was taken assuming the first exposure occurred at $t = 0$.

Our faintest object, 2MA 2244, does not show an increase in its brightness with time for the Ch. 4 photometry, and thus, we did not apply the correction to this object. The difference in the latent behavior in this case is probably due to the different frame times used for this object and the fact that two repeats of 50 s each are used to synthesize a 100 s frame. Different frame times have slightly different commanding that leads to small differences in the delay between consecutive integrations. It is possible that 2MA 2244 does not show a significant latent buildup
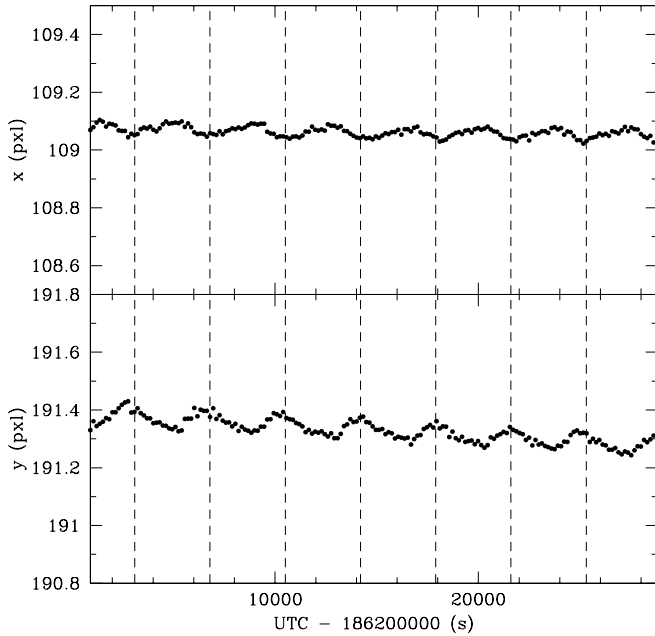
FIG. 5.—Array x-position (top) and y-position (bottom) as a function of time for 2MA 0908. Both positions oscillate with a period of ∼3000 s. Small heaters near the star tracker cycle their power with a similar period and are likely producing flexure in the trackers.

because the latent images are sensitive to such delays. The dependence of latent charge buildup as a function of position on the array, frame time, and flux would have to be studied before a more accurate correction could be applied.

5.3. Periodic Movement of the Pointing

Since the observation of 2MA 0908 was performed under only one AOR, it gave us the opportunity to study the pointing without the large shifts introduced by the change of AORs. In this case, the movement of the x- and y-positions with time showed a sawtooth pattern with a period of 3000 s and a peak-to-peak amplitude of 0.1 pixels (see Fig. 5), with the largest amplitude in the y-axis of the array. There is also a slow, approximately linear drift in the y-axis position, amounting to approximately 0.1 pixels over the 8 hr period of the observation.

We examined the pointing history file for the time period while our targets were being observed and there was no measurable telescope oscillation. There is a small, approximately constant drift in right ascension during the observation, and a small pointing discontinuity when a new AOR starts, but we do not see the 3000 s period that we see with the IRAC data. There are temperature sensors attached to the cold plate on which IRAC is mounted. The sensors indicate an oscillation in temperature with a similar period. The heaters located near the star tracker could be cycling on and off, causing the tracker to bend slightly, and that could be a plausible cause for this effect. In any case, the effect of this oscillation on the light curves is very small, and it should be fixed with the pixel-phase correction applied.

5.4. The Corrected Photometry

Figure 6 shows the light curves of the three targets, corrected for the effects of pixel phase and latent image buildup. The top and bottom panels show the Ch. 2 and Ch. 4 data, respectively. The rms error is represented by an error bar at the lower left corner of each panel. After applying the pixel-phase correction to Ch. 2 data, discontinuities between AORs are no longer visible.
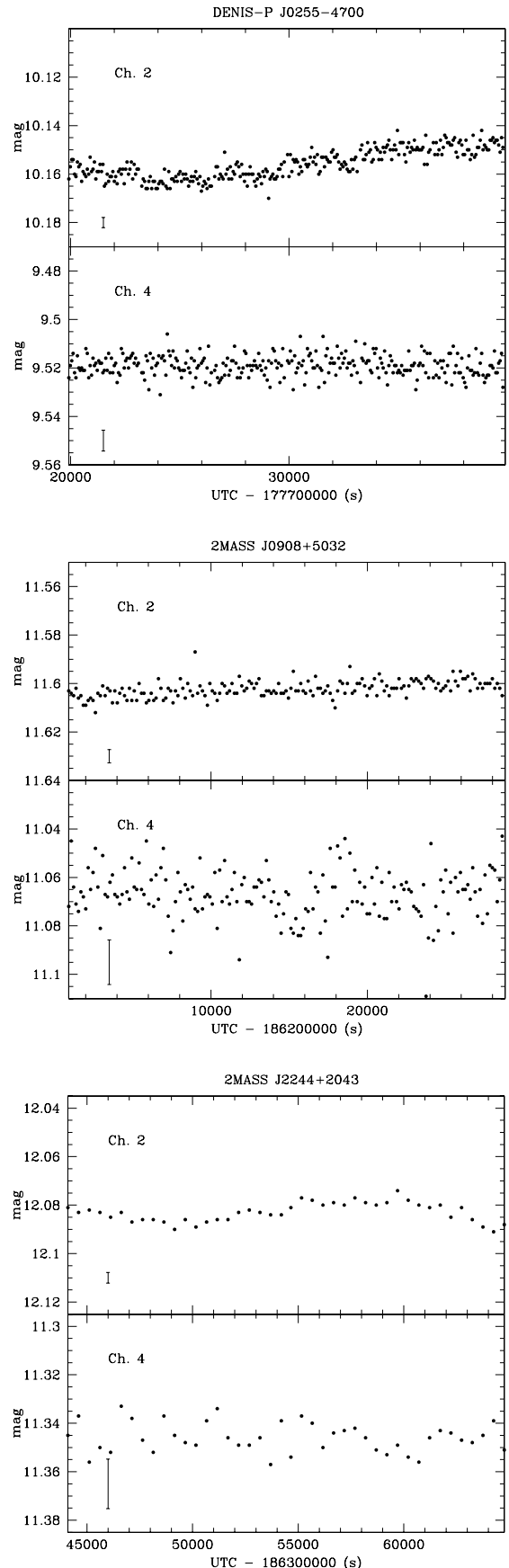

FIG. 6.—Final light curves for DENIS 0255, 2MA 0908, and 2MA 2244. All three have been corrected from pixel phase at Ch. 2 (top), and DENIS 0255 and 2MA 0908 have been corrected from latent images at Ch. 4 (bottom). The 1 σ per point uncertainty is represented in the lower left corner of each panel.

TABLE 4
MAIN RESULTS FOR THE THREE TARGETS

	4.5 μm				8 μm			
OBJECT	mag	rms	p	$T_{\rm rot}$ (hr)	mag	rms	p	$T_{\rm rot}$ (hr)
DENIS 0255	10.156 ± 0.002	0.006	$<10^{-4}$	7.4	9.519 ± 0.004	0.004	0.3	...
2MA 0908.................	11.602 ± 0.003	0.003	0.07	...	11.067 ± 0.009	0.009	0.22	...
2MA 2244.................	12.083 ± 0.004	0.004	0.003	4.6	11.346 ± 0.006	0.006	0.4	...

The photometry of two brightest objects, DENIS 0255 and 2MA 0908, were corrected for latent images in Ch. 4 (2MA 2244 did not show that effect probably due to its faintness and different frame time) and now appear flat. Note that the trends in both bandpasses are different and that, at least for DENIS 0255 and 2MA 0908, there is a lack of photometric modulation at the expected rotational periods. The rms of the light curves are 6 and 4 mmag for Ch. 2 and Ch. 4, respectively, for DENIS 0255, 3 and 9 mmag for 2M0908, and 4 and 8 mmag for the faintest object, 2MASS 2244. Therefore, any possible variability on the timescale of 6 or 8 hr would be less than these values.

6. ANALYSIS OF VARIABILITY

The data of each brown dwarf were analyzed in a similar way to that of Bailer-Jones & Mundt (1999). The χ^2 test was used to determine the probability that the deviations in the light curve are consistent with the photometric errors (i.e., nonvariable). The null hypothesis for the test is that there is no variability. We evaluated the χ^2 statistic,

$$\chi^2 = \sum_{k=1}^{k=K} \left[\frac{\Delta m(k)}{\sigma} \right]^2, \qquad (5)$$

where K is the number of data points in the light curve, $\Delta m(k)$ is the magnitude for each data point with the mean magnitude subtracted, and σ is the rms error.

A large χ^2 value indicates a greater deviation compared to the errors and thus a smaller probability that the null hypothesis is true (i.e., variable). This probability, p, is calculated, and we claim evidence for variability if $p < 0.01$ (a 2.5 σ detection). This method is very sensitive to the accuracy of the errors. We believe that the technique used to estimate the errors (obtained empirically from the data themselves) has the advantage that false detections associated with underestimating the errors can be avoided.

If evidence of variability was found in an object, we looked for a periodic signal in the data following the methodology described by Scargle (1982). This method is equivalent to a least-squares fit (in the time domain) of sinusoids to the data. The algorithm calculates the normalized Lomb periodogram for the data and gives us a false-alarm probability based on the peak height in the periodogram as a measure of significance.

We also examined carefully the data in order to identify any possible signal that could be interpreted as the result of a brown dwarf flare. However, only single-point (before binning) deviants—presumably radiation events in the detector—were found.

7. RESULTS AND DISCUSSION

7.1. DENIS-P J0255−4700

DENIS-P J0255−4700 is the brightest member of our sample. That and its late L spectral type make this target perfect for this study. Furthermore, it is one of the best-studied objects in the late L/early T region. It has been claimed to be variable in the Ic band on more than one timescale (Koen 2005), but on the other hand, no signs of variability have been found in any other band. This object has a $v \sin i$ of ~ 40 km s^{-1} (Basri et al. 2000; Zapatero Osorio et al. 2006), and hence, its rotation period should be of 3 hr or less, and our 6 hr of continuous observation should capture two full periods.

Table 4 shows main results for all targets including IRAC magnitudes, rms amplitudes, probability of an object to be nonvariable, and period of the modulation observed. This object was labeled as variable in Ch. 2 ($p \le 10^{-4}$) and nonvariable in Ch. 4 ($p = 0.3$) by the criteria used. However, if any variability is present, it has to be under a rms amplitude of 6 mmag for Ch. 2 and 4 mmag for Ch. 4 (see top panel of Fig. 6). The periodogram searches for periods in the interval ranging from that corresponding to the Nyquist frequency (~ 3 minutes) to values slightly larger than the interval covered by our observations. The power spectrum of this object shows only one strong peak at 7.4 hr, almost twice the period predicted from the spectroscopic rotational velocity. Hence, the cause of variability would have to be some type of global change in the luminosity of the object (which for some reason is not modulated on the rotation period). Future observations would be useful in order to determine if any kind of long-term variability is present. Another possibility would be that the $v \sin i$ is in error or that our assumed radius is in error (in both cases by of order a factor of 2). However, recently Zapatero Osorio et al. (2006) have derived the same $v \sin i$ with higher accuracy by using Keck NIRSPEC IR spectrograph. DENIS 0255 does not show any evidence of lower gravity in its optical spectrum or near-IR colors, and thus, nothing indicates that it has a larger than normal radius (as might be the case if it were very young). Note that our 6 hr of observation do not allow us to see an entire phase, and thus, we cannot check the validity of the estimated period.

We note that our DENIS 0255 observations had by far the largest movement in the stellar centroid during the observing period of our three targets. We know that there are instrumental effects that depend on position on the array (both pixel-phase effects and flat-field errors) that affect the measured flux in Ch. 2, and those effects are smaller for Ch. 4. Therefore, even having removed the instrumental effects, the most likely object for us to see a spurious signal for was DENIS 0255, and we should have seen it to be larger in Ch. 2—exactly as was the case.

On the other hand, the fact that we see variations in Ch. 2 and not in Ch. 4 is not inconsistent with the hypothesis of real variability arising from clouds. The spectra of L and T dwarfs are sculpted by molecular absorption bands that vary greatly in strength as a function of wavelength. Thus, there is no well-defined "photosphere," and the depth from which flux is emitted varies strongly with wavelength. Assuming a well-defined cloud layer, flux may originate from above, within, or even (for small optical

depths) from below the cloud layer (Ackerman & Marley 2001). Thus, if a local hole suddenly appears in an otherwise uniform, global cloud deck, it will only be apparent at those wavelengths that would otherwise originate from within or below the cloud. The presence of the hole would not be apparent in spectral regions originating from well above the cloud deck. This effect is well known from observations of Jupiter. The "five micron hot spots" (Westphal et al. 1974) of Jupiter arise from holes in the global ammonia cloud deck, allowing flux from hotter, deeper seated regions to escape to space. The hot spots are apparent at 5 μm because this is a region of relatively low molecular opacity. These hot spots are not apparent at longer wavelengths where flux originates from higher in the atmosphere.

Among the IRAC bandpasses, Ch. 1 and 2 (3.6 and 4.5 μm) probe most deeply into late L dwarf atmospheres. Because they overlap regions of higher molecular (primarily water and carbon monoxide) opacity, Ch. 3 and 4 (5.8 and 8 μm) probe higher in the atmosphere, generally above the region cloud models predict is occupied by the iron and silicate clouds (Ackerman & Marley 2001; M. S. Marley 2006, in preparation). All else being equal, we expect any variability arising from nonuniform cloud coverage to be greatest in Ch. 1 and 2. If the dispersions observed in the Ch. 2 data do in fact arise from atmospheric variability, we predict that comparable or larger variations would be detectable in Ch. 1, but not Ch. 3.

Whether the 7.4 hr modulation in Ch. 2 is instrumental in origin or intrinsic to the target, our data place a limit on the amplitude for a true rotational modulation with a period between 20 minutes and 6 hr below 6 mmag for this channel.

7.2. *2MASS J0908+5032*

This object has very discrepant optical and near-infrared spectral types that could indicate a cloudy atmosphere. Its $v \sin i$ is 31 km s^{-1}; thus, its period should be less than 4 hr, and our observation would again obtain two whole periods.

A glance at the light curve of 2MASS 0908 should be enough to convince the reader that coherent rotational modulation is not present. This object shows no prominent features in its light curve more than a very slight increment of its brightness along the whole observation period for Ch. 2. Again this pattern is not confirmed by the Ch. 4 data, and thus, it seems that some other cause, aside from intrinsic variability, is responsible for the feature. The χ^2 test labels this object as nonvariable in both channels. Any possible variability over the 8 hr is at or below the 3 and 9 mmag level in Ch. 2 and Ch. 4, respectively.

7.3. *2MASS J2244+2043*

The object 2MASS J2244+2043 is an L7.5 brown dwarf, with very red near-infrared colors that could be indicative of dust in its atmosphere. We do not have a measure of the $v \sin i$, but based on the mean $v \sin i$ for L dwarfs, we expect a rotational period of approximately 6.5 hr or less. 2MA 2244 is the faintest object in our sample.

The results of the χ^2 test indicate variability in Ch. 2 and no variability in Ch. 4. Again, as in DENIS 0255, the Ch. 4 data do not show the same trend. Indeed, its light curve at Ch. 2 (bottom panel in Fig. 6) shows a small-amplitude, approximately sinusoidal modulation. If the variation is intrinsic to the target, a feature in the brown dwarf's atmosphere, or some differences in the cloud covering fraction could be causing it. However, such differences should be very small, since the rms amplitude of the light curve is only 4 mmag. The periodogram of this object shows again only one strong peak at 4.6 hr. This value is consistent with the range of rotation periods expected for this object. However,

note that even though the variations of the centroid for this object are much smaller than those of DENIS 0255, there was still a bump of 0.3 pixels in the transition of AORs (just in the middle of the observation period).

7.4. *Limits on Nonaxisymmetric Cloud Distributions for Our Targets*

Atmospheric clouds (or other surface inhomogeneities) affect the observed photometry due to the lower luminosity of the cloud in comparison with that of a free-cloud region of equivalent size. We have made a simple model to constrain the size of the feature that could be causing the observed variability (other models have been presented by Clarke et al. [2003] and Bailer-Jones [2002]). The proposed scenario is an L8 brown dwarf with a small inclination to the line of sight and a spot or group of spots at low latitude in its atmosphere. We assume that, if the cloud deck starts to break up, the cloud-free parts would have spectral characteristics like those of an early T dwarf. Assuming typical J−[Ch. 2] colors for both kind of objects, we can derive the difference in brightness and hence the approximate size of the spot that could be causing the observed amplitude. From DENIS 0255 data, we can say that the maximum photometric amplitude of a half-sine-wave light curve would be 6 mmag in Ch. 2, and hence, at this level of approximation, we can place a rough limit of a spot size of ∼1% of the visible hemisphere of the object. The same calculation for 2MA 2244 leads to a limit of a spot size of ∼2% of the visible hemisphere.

8. SUMMARY AND CONCLUSIONS

We have conducted a photometric monitoring program of three late L brown dwarfs at the Ch. 2 (4.5 μm) and Ch. 4 (8 μm) bandpasses with observations that lasted for one or two rotational periods of the object. This project presents the most sensitive search yet obtained for brown dwarf mid-IR variability. The observational mode selected allowed us to obtain very well sampled light curves in the time domain and 1 σ rms uncertainties of <3 mmag in Ch. 2 and around 9 mmag in Ch. 4. For each target brown dwarf, the search was sensitive to the timescale of our observations (6 or 8 hr depending on the object), and hence, larger variability on timescales to which we were not sensitive could be present.

Two out of the three objects studied exhibit some variation in their light curves. DENIS 0255 turned out to be variable in Ch. 2 according to the χ^2 test, with a 99% confidence level. A period of 7.4 hr was derived using the normalized Lomb periodogram. If this variability is real and is a rotational modulation, its period would be much larger than the rotational period and would have a peak-to-peak amplitude of 10 mmag. The cause of variability could also be some type of global longer term change in the luminosity of the object, which for some reason is not modulated on the rotation period. The fact that some instrumental effects that could affect the photometry at Ch. 2 were larger in DENIS 0255 than in any other object suggests that perhaps the variability is not real. The Ch. 4 data show a flat light curve with no possible variability over the 4 mmag level. However, since the flux at the two bandpasses arises from different vertical regions in the atmosphere, the different shapes in the light curves for Ch. 2 and Ch. 4 are consistent with the hypothesis of variability caused by clouds in the atmosphere of the L dwarf; 2MA 2244 was also labeled as variable by χ^2 test. In this case, its derived period of 4.6 hr is compatible with the expected rotational period. This photometric modulation would have a peak-to-peak amplitude of 8 mmag. Note that the expected period for this object

comes from a mean $v \sin i$ for L dwarfs, and thus we cannot prove that there is a rotational modulation with these data. Again the feature is not confirmed by the Ch. 4 data (which shows no variability over 8 mmag), and even though the instrumental effects present in the data were smaller for this object, some of them could still remain after the corrections; 2MA 0908 did not show any rotational modulation in its light curve, and no other type of variability is present either. Hence, we found no variability with limits of 3 and 9 mmag in Ch. 2 and Ch. 4, respectively.

If we assume that the DENIS 0255 and 2MA 2244 are variable, our simple model puts an upper limit on the size of the feature in ~1%–2% of the visible hemisphere of the object. If instead, the variability shown by our targets has an instrumental origin, our nonvariable L dwarfs could be either completely covered with clouds or objects whose clouds are smaller and uniformly distributed along its atmosphere. Such scenarios would lead to very small photometric variations. Follow-up photometry in IRAC Ch. 1 and Ch. 3 should distinguish between instrumen-

tal and intrinsic sources of variability. If the variations arise on the targets, then the amplitude of the variations should vary between bandpasses in a manner consistent with the atmospheric condensate structure (Ackerman & Marley 2001) and still be consistent with the rotational period implied by our observations.

Facilities: Spitzer (IRAC)

REFERENCES

Ackerman, A. S., & Marley, M. S. 2001, ApJ, 556, 872
Bailer-Jones, C. A. L. 2002, A&A, 389, 963
———. 2004, A&A, 419, 703
Bailer-Jones, C. A. L., & Lamm, M. 2003, MNRAS, 339, 477
Bailer-Jones, C. A. L., & Mundt, R. 1999, A&A, 348, 800
———. 2001, A&A, 367, 218
Basri, G., et al. 2000, ApJ, 538, 363
Burgasser, A. J., et al. 2002, ApJ, 571, L151
Chabrier, G., & Baraffe, I. 1997, A&A, 327, 1039
Charbonneau, D., et al. 2005, ApJ, 626, 523
Clarke, F. J., Oppenheimer, B. R., & Tinney, C. G. 2002a, MNRAS, 335, 1158
Clarke, F. J., Tinney, C. G., & Covey, K. R. 2002b, MNRAS, 332, 361
Clarke, F. J., Tinney, C. G., & Hodgkin, S. T. 2003, MNRAS, 341, 239
Cruz, K. L., Reid, I. N., Liebert, J., Kirkpatrick, J. D., & Lowrance, P. J. 2003, AJ, 126, 2421
Dahn, C. C., et al. 2002, AJ, 124, 1170
Enoch, M. L., Brown, M. E., & Burgasser, A. J. 2003, AJ, 126, 1006
Fazio, G. G., et al. 2004, ApJS, 154, 10
Gelino, C. R. 2002, Ph.D. thesis, New Mexico State Univ.

Gelino, C. R., Marley, M. S., Holtzman, J. A., Ackerman, A. S., & Lodders, K. 2002, ApJ, 577, 433
Kirkpatrick, J. D. 2005, ARA&A, 43, 195
Knapp, G. R., et al. 2004, AJ, 127, 3553
Koen, C. 2003, MNRAS, 346, 473
———. 2005, MNRAS, 360, 1132
Koen, C., Matsunaga, N., & Menzies, J. 2004, MNRAS, 354, 466
Koen, C., Tanabé, T., Tamura, M., & Kusakabe, N. 2005, MNRAS, 362, 727
Liu, M. 2006, ApJ, 647, 1393
Maiti, M., Sengupta, S., Parihar, P. S., & Anupama, G. C. 2005, ApJ, 619, L183
Meyer, M. R., et al. 2004, ApJS, 154, 422
Mohanty, S., & Basri, G. 2003, ApJ, 583, 451
Reach, W. T., et al. 2005, PASP, 117, 978
Scargle, J. D. 1982, ApJ, 263, 835
Tinney, C. G., & Tolley, A. J. 1999, MNRAS, 304, 119
Tsuji, T., & Nakajima, T. 2003, ApJ, 585, L151
Vrba, F. J., et al. 2004, AJ, 127, 2948
Westphal, J. A., Matthews, K., & Terrile, R. J. 1974, ApJ, 188, L111
Zapatero Osorio, M. R., et al. 2006, ApJ, 647, 1405